LBNL-57002

Effects of Cerium Incorporation into Zirconia on the Activity of Cu/ZrO_2 for Methanol Synthesis via CO Hydrogenation

Konstantin A. Pokrovski, Michael D. Rhodes and Alexis T. Bell*

Chemical Sciences Division
Lawrence Berkeley National Laboratory
and
Department of Chemical Engineering
University of California
Berkeley, CA 94720-1462

Submitted to
Journal of Catalysis

August 24, 2005

Author to whom correspondence should be addressed: **bell@cchem.berkeley.edu**

Abstract

The effects of Ce incorporation into ZrO_2 on the catalytic performance of Cu/ZrO_2 for the hydrogenation of CO have been investigated. A $Ce_{0.3}Zr_{0.7}O_2$ solid solution was synthesized by forced hydrolysis at low pH. After calcination at 873 K, XRD and Raman spectroscopy characterization indicated that the $Ce_{0.3}Zr_{0.7}O_2$ had a t´´ crystal structure. 1.2 wt% $Cu/Ce_{0.3}Zr_{0.7}O_2$ exhibited H_2 consumption peaks at low temperature (< 473 K) during H_2-TPR indicating a significant fraction (~ 70%) of Ce^{4+} is reduced to Ce^{3+}. 1.2 wt% $Cu/Ce_{0.3}Zr_{0.7}O_2$ is 2.7 times more active for methanol synthesis than 1.2 wt% $Cu/m\text{-}ZrO_2$ at 3.0 MPa at temperatures between 473 and 523 K and exhibits a higher selectivity to methanol. *In-situ* infrared spectroscopy shows that, analogous to $Cu/m\text{-}ZrO_2$, the primary surface species on $Cu/Ce_{0.3}Zr_{0.7}O_2$ during CO hydrogenation are formate and methoxide species. A shift in the band position of the bridged methoxide species indicated that some of these groups were bonded to both Zr^{4+} and Ce^{3+} cations. For both catalysts, the rate-limiting step for methanol synthesis is the reductive elimination of methoxide species. The higher rate of methanol synthesis on $Cu/Ce_{0.3}Zr_{0.7}O_2$ relative to $Cu/m\text{-}ZrO_2$ was primarily due to a ~ 2.4 times higher apparent rate constant, k_{app}, for methoxide hydrogenation, which is attributed to the higher surface concentration of H atoms on the former catalyst. The increased capacity of the Ce-containing catalyst is attributed to interactions of H atoms with Ce-O pairs present at the surface of the oxide phase.

Introduction

Several studies have indicated that support composition affects the activity of Cu-based catalysts for CO hydrogenation to methanol [1-6]. Zirconia has proven to be a particularly promising support for such applications, since Cu/ZrO_2 catalysts can be operated with or without the presence of CO_2 [7-11]. Mechanistic studies have shown that for such catalysts CO adsorbs preferentially on the surface of zirconia to form formate species which then undergo hydrogenation to produce methanol. The hydrogen atoms required for this process are produced by dissociative adsorption of H_2 on the surface of the dispersed Cu and then spillover onto the zirconia surface. Recent work by Bell and co-workers [12, 13] has demonstrated that the phase of zirconia can also influence catalyst activity. Thus, $Cu/m\text{-}ZrO_2$ ($m\text{-}ZrO_2$ – monoclinic zirconia) was shown to be nearly an order of magnitude more active for methanol synthesis than $Cu/t\text{-}ZrO_2$ ($t\text{-}ZrO_2$ – tetragonal zirconia) for equivalent zirconia surface areas and surface concentrations of dispersed Cu. This difference is attributed primarily to the presence of oxygen vacancies on the surface of $m\text{-}ZrO_2$, which facilitate the reaction of CO with neighboring hydroxyl groups to generate formate species and provide additional sites for hydrogen activation and storage. These properties result in higher CO adsorption capacities and higher rates of reductive elimination of methoxide species on $Cu/m\text{-}ZrO_2$ relative to $Cu/t\text{-}ZrO_2$. Since the availability of atomic H on the surface of zirconia is essential for the hydrogenation of adsorbed CO, a motivation exists for exploring means for increasing the hydrogen adsorption capacity of zirconia.

CeO_2 has been utilized in automotive three-way catalysts to serve as an oxygen-buffering component during rich/lean oscillations of exhaust gases [14-18]. The ability

of CeO_2 to either donate its oxygen or adsorb and store oxygen derived from molecular sources stems from the facile, reversible redox cycle $Ce^{4+} \rightleftarrows Ce^{3+}$. Reduction of CeO_2 to CeO_{2-x} stoichiometries results in the generation of oxygen vacancies throughout the oxide lattice. Incorporation of Zr^{4+} into the CeO_2 lattice enhances reducibility and increases the oxygen-storage capacity of the solid solution [14, 15, 17, 19]. Spectroscopic studies suggest the coordination number of the smaller Zr ion decreases in the mixed oxide, increasing oxygen mobility and the creation of vacancies [20].

The present study was undertaken to examine the influence of Ce incorporation into ZrO_2 on the catalytic activity of $Cu/Ce_xZr_{1-x}O_2$ for methanol synthesis from CO/H_2. ZrO_2 and $Ce_{0.3}Zr_{0.7}O_2$ were prepared by forced hydrolysis at low pH and Cu was dispersed on the surface of these materials by deposition precipitation. Catalysts were characterized by XRD, Raman spectroscopy, temperature-programmed reduction (TPR) in H_2, and catalyst H_2 and CO adsorption capacities were measured by temperature-programmed desorption (TPD). Steady-state catalytic performance measurements were supplemented with dynamic surface studies using *in-situ* infrared spectroscopy.

Experimental

Catalyst Preparation

ZrO_2 was prepared by boiling a 0.5 M solution of zirconyl chloride ($ZrOCl_2 \cdot 8H_2O$, 99.99%, Aldrich) under reflux for 240 h. The final solution had a pH < 1. NH_4OH was added dropwise to agglomerate the resulting fine particles to facilitate their filtration. The recovered precipitate was washed and redispersed in deionized water several times to remove residual chlorine. $AgNO_3$ was used to test the filtrate for any

remaining Cl anions. The material was then dried in air at 383 K overnight prior to calcination. $Ce_{0.3}Zr_{0.7}O_2$ was prepared by boiling a 0.5 M solution (total metals basis) of zirconyl nitrate ($ZrO(NO_3)_2 \cdot 6H_2O$, 99.99% Aldrich) and cerium(III) nitrate ($Ce(NO_3)_3 \cdot 6H_2O$, 99.999%, Aldrich) under reflux for 240 h. The final solution had a pH < 1. NH_4OH was added dropwise to agglomerate the resulting fine particles to facilitate their filtration. The precipitated material was washed and then dried overnight prior to calcination. Each sample was calcined in dry air flowing at 100 cm^3/min. The temperature was ramped from room temperature at a rate of 2 K/min to the final temperature, which was maintained for 3 h. The ZrO_2 and $Ce_{0.3}Zr_{0.7}O_2$ samples were calcined at 738 and 873 K, respectively. 1.2 wt% Cu/ZrO_2 catalysts were prepared with each calcined support by deposition precipitation. Details of this preparation have been described previously [12].

Prior to testing or characterization, each catalyst sample was calcined in a 10% O_2/He mixture flowing at 60 cm^3/min. The sample was heated from room temperature to 573 K at 0.5 K/min and then maintained at 573 K for 2 h. The sample was then cooled to 323 K, swept with He, and then reduced in a 10% H_2/He mixture flowing at the rate of 60 cm^3/min while the temperature was increased at the rate of 2 K/min up to 573 K. The flow of 10% H_2/He was maintained at 573 K for 1 h prior to switching to a flow of 100% H_2 for an additional 1 h.

Catalyst Characterization

The crystallographic phase of each material was determined by both X-ray diffraction and Raman spectroscopy. XRD patterns were obtained with a Siemens D5000 diffractometer, which uses Cu-Kα radiation and a graphite monochrometer. Scans were

made in the 2θ range of 10 to 120° with a step size of 0.02° and a time/step of 11 s. Rietveld refinement was performed using EXPGUI GSAS software [21]. Raman spectra were recorded with a HoloLab 5000 Raman spectrometer (Kaiser Optical) at room temperature at resolution 2 cm^{-1}. The stimulating light source is a Nd:YAG laser, the output of which is frequency doubled to 532 nm. Laser power at the sample was approximately 20 mW.

The BET surface area of each ZrO_2 support was determined using an Autosorb 1 (Quantachrome Instruments) gas adsorption system with nitrogen adsorption/desorption isotherms. Prior to each analysis, samples were dried at 393 K under vacuum for > 2 h. BET surface areas were calculated using a 5-point isotherm. After calcination the surface areas of ZrO_2 and $Ce_{0.3}Zr_{0.7}O_2$ were 143 m^2/g and 120 m^2/g, respectively.

The concentration of exchangeable hydrogen on each sample was quantified using H/D exchange. Fully reduced samples were purged with He at 298 K for 30 min followed by ramping the temperature at 20 K/min from 298 K to 623 K in 40 cm^3/min of D_2. Both HD and H_2 evolution were monitored using a mass spectrometer (Minilab, Spectra Products), but only HD generation was observed. For each sample, exchange was complete by ~ 523 K.

H_2-TPR studies were conducted using 0.15 g of a calcined sample purged with He at 298 K for 30 min. The flow was then switched to 2% H_2/He at a flow rate of 60 cm^3/min and then ramped from 298 K to 673 K while monitoring H_2 consumption using a mass spectrometer. Cu surface areas were quantified using N_2O titrations followed by H_2-TPR [22]. A value of 1.46×10^{19} Cu atoms/m^2 and a stoichiometry of 2 Cu/H_2 was utilized [23].

Adsorption capacities for H_2 and CO and were determined using temperature-programmed desorption (TPD). In the case of H_2 the sample was calcined and reduced at 573 K. The sample was then cooled in H_2 to 298 K and purged in He. Desorption was conducted by ramping the sample temperature at 20 K/min from 298 K to 773 K in flowing He while monitoring the desorbing gas using a mass spectrometer. To determine the CO adsorption capacity, the sample was calcined and reduced and then cooled to 523 K and flushed with He for 30 min. 4.0% CO/He was then flowed over the catalyst at a flow rate of 60 cm^3/min for 20 min. The sample was then cooled to 298 K in 4.0% CO/He before being purged with He to remove any weakly adsorbed species. Desorption of adsorbed CO was carried out in a manner identical to that used for adsorbed H_2.

Catalyst Testing

Activity and selectivity measurements for CO hydrogenation were carried out in a continuous flow, fixed-bed reactor. Details of the apparatus have been described previously [12]. Reactions were carried out with 0.15 g of catalyst at a pressure of 3.0 MPa. Total reactant gas flow was 60 cm^3/min with a H_2/CO ratio of 3/1. Product gas mixtures were analyzed after 2 h on stream at a given temperature. Temperature was then ramped to the successive temperature at a rate of 2 K/min. Conversion and selectivity were referenced to CO, the limiting reactant.

Infrared Spectroscopy Studies

In-situ transmission infrared spectroscopy experiments were conducted using a low dead volume infrared cell with CaF_2 windows [24]. Infrared spectra were recorded with Magna 750 Series II IR spectrometer (Nicolet) at resolution $2cm^{-1}$. In an effort to remove any residual surface species prior to testing, each sample was calcined in a 10%

O_2/He mixture flowing at 60 cm^3/min. The sample was heated from room temperature to 523 K at 2 K/min and then maintained at 523 K for 8 h. The sample was then cooled to 323 K, swept with He, and then reduced in a 10% H_2/He mixture flowing at the rate of 60 cm^3/min while the temperature was increased at the rate of 2 K/min up to 523 K. The flow of 10% H_2/He was maintained at 523 K for 1 h prior to switching to a flow of 100% H_2 for an additional 1-3 h. The sample was then flushed with He for 1 h preceding sample testing.

Results and Discussion

Material Characterization of ZrO_2 Supports

XRD patterns of the ZrO_2 and $Ce_{0.3}Zr_{0.7}O_2$ are shown in Figure 1. The diffraction pattern for ZrO_2 exhibits peaks characteristic of monoclinic ZrO_2 (m-ZrO_2). The occurrence of pure monoclinic ZrO_2 was confirmed by Rietveld refinement in the monoclinic symmetry, $P2_1/c$ (Fig. 1d and 1e). The XRD pattern for $Ce_{0.3}Zr_{0.7}O_2$ exhibits a primary diffraction peak centered at $2\theta \sim 30^o$ characteristic of both the tetragonal and cubic phases of ZrO_2 (t-ZrO_2, c-ZrO_2) (Fig. 1a). The position of the main peak $Ce_{0.3}Zr_{0.7}O_2$ occurs at 29.5º, as opposed to 30.2º for t-ZrO_2, c-ZrO_2, consistent with an increase in the lattice cell parameter upon the substitution of Zr^{4+} (radius 0.86 Å) by Ce^{4+} cations (radius 0.97 Å). The symmetry of the diffraction peaks and the absence of features associated with CeO_2 suggest the formation of a $Ce_xZr_{1-x}O_2$ solid solution [25, 26]. The thermodynamically stable phase of $Ce_xZr_{1-x}O_2$ solutions is monoclinic for Zr-rich compositions (< 10 at% Ce) and cubic for Ce-rich compositions (> 80 at% Ce) [27, 28]. Intermediate compositions are reported to exhibit a number of stable and metastable

phases of tetragonal symmetry [29-31]. The phase of $Ce_{0.3}Zr_{0.7}O_2$ was analyzed by Rietveld refinement of the measured diffraction pattern. Refinement was performed in both cubic ($Fm3m$, $a = 5.20$ Å) and tetragonal ($P4_2/nmc$, $a = 3.68$, $c = 5.19$, $a_f/c = 1.00(3)$, where $a_f = a\sqrt{2}$) symmetries (Fig. 1b and 1c, respectively). The broadness of the diffraction peaks made it impossible to identify the displacement of oxygen ions from their ideal fluorite positions by Rietveld refinement; hence, a more definitive assessment of the crystalline structure of $Ce_{0.3}Zr_{0.7}O_2$ was attempted using Raman spectroscopy [32].

The Raman spectra of ZrO_2 and $Ce_{0.3}Zr_{0.7}O_2$ are presented in Figure 2. ZrO_2 exhibits peaks at 182 cm^{-1}, 333 cm^{-1}, 377 cm^{-1}, 475 cm^{-1}, 559 cm^{-1}, and 623 cm^{-1}, which are characteristic of m-ZrO_2 [33-35]. Thus both XRD and Raman spectroscopy confirm that the ZrO_2 sample is m-ZrO_2. The $Ce_{0.3}Zr_{0.7}O_2$ sample exhibits a principle peak at 474 cm^{-1}, and two smaller peaks at 316 and 621 cm^{-1}. The peak at 474 cm^{-1} is characteristic of a cubic fluorite structure [36, 37]. However, the presence of peaks at 316 and 621 cm^{-1} and the absence of the characteristic tetragonal peak at ~ 275 cm^{-1} indicate that $Ce_{0.3}Zr_{0.7}O_2$ is in the t´´ phase [29]. This phase is intermediate between the tetragonal and cubic phases, in which the oxygen atoms are displaced from the positions of these atoms in an ideal fluorite structure. While the t´´ phase is commonly reported to exist at Ce compositions between 65-80 at% [29], other authors have reported the generation of this phase at lower Ce contents for small particles [38, 39].

Material Characterization of Cu/m-ZrO_2 and Cu/ t´´-$Ce_{0.3}Zr_{0.7}O_2$

A loading of 1.2 wt% Cu was deposited onto ZrO_2 and $Ce_{0.3}Zr_{0.7}O_2$. The Cu surface area and associated dispersion for each sample are given in Table 1. The Cu

particles dispersed on m-ZrO_2 had a slightly higher overall Cu surface area, but each catalyst had a very similar Cu surface area to support surface area ratio. The surface concentration of exchangeable hydrogen, quantified by H/D exchange, for each sample is also listed in Table 1. *In-situ* infrared studies have shown that this quantity is indicative of the concentration of hydroxyl groups on the catalyst surface [40-41]. The surface concentration of OH groups was ~ 40% higher on 1.2 wt% Cu/m-ZrO_2 than 1.2 wt% Cu/$Ce_{0.3}Zr_{0.7}O_2$. The infrared spectrum of the O-H stretching region after calcination and reduction are shown in Figure 3 for 1.2 wt% Cu/m-ZrO_2 and 1.2 wt% Cu/$Ce_{0.3}Zr_{0.7}O_2$. Spectra were referenced to the empty cell in He. Each sample exhibits two types of isolated hydroxyl groups (> 3600 cm^{-1}). Despite a crystal structure that is pseudo tetragonal/cubic, the peak positions of 1.2 wt% Cu/$Ce_{0.3}Zr_{0.7}O_2$ (3670 and 3731 cm^{-1}) are very similar to those for 1.2 wt% Cu/m-ZrO_2 (3668 and 3729 cm^{-1}). Analogous to 1.2 wt% Cu/m-ZrO_2, 1.2 wt% Cu/t´´-$Ce_{0.3}Zr_{0.7}O_2$ exhibits a higher relative concentration of low-frequency hydroxyl groups. The positions of these features are similar to those reported previously for OH bands on t-ZrO_2 and m-ZrO_2 [39-41]. While the exact positions of such bands can depend on the degree of surface hydroxylation, the higher frequency band is commonly assigned to terminal hydroxyl groups and the lower frequency band, to either bi- or tri- bridging groups [40, 42]. Recent theoretical studies of the surfaces of both ZrO_2 polymorphs also lead to the conclusion that a combination of terminal and both bi- and tribridged OH groups should be present [43-46].

The H_2-TPR profile for each catalyst is given in Figure 4. 1.2 wt% Cu/m-ZrO_2 exhibited one principle peak with a maximum at 473 K, attributed to the reduction of highly dispersed CuO or Cu^{2+} ions in an octahedral environment [42, 43]. The amount of

H_2 consumed was slightly greater than the value corresponding to the complete reduction of CuO species (H_2/CuO ~ 1.1). 1.2 wt% Cu/t´´-$Ce_{0.3}Zr_{0.7}O_2$ exhibited a significantly larger consumption of H_2 due to the reduction of Ce^{4+} to Ce^{3+}. If the H_2/CuO ratio is assumed to be ~ 1, the additional H_2 consumption corresponds to a reduction of ~ 70 % of the Ce atoms in the support. Reduction occurs with two primary peaks at 403 K and 443 K. The presence of either noble or base metals facilitate reduction of Ce due to spillover of H atoms from the metal surface [44-46]. Similar reduction peaks have been reported during H_2-TPR with CuO/$Ce_{0.44}Zr_{0.56}O_2$ [47].

Table 2 lists the H_2 and CO adsorption capacities of 1.2 wt% Cu/m-ZrO_2 and 1.2 wt% Cu/t´´-$Ce_{0.3}Zr_{0.7}O_2$ determined from TPD spectra. The amount of H_2 adsorbed per unit area is 3.3 times higher for 1.2 wt% Cu/t´´-$Ce_{0.3}Zr_{0.7}O_2$ relative to that for 1.2 wt% Cu/m-ZrO_2. While the total amount of CO adsorbed is significantly higher than the amount of H_2 adsorbed on both catalysts, the ratio of CO adsorbed on 1.2 wt% Cu/t´´-$Ce_{0.3}Zr_{0.7}O_2$ relative to that on 1.2 wt% Cu/m-ZrO_2 is only a factor of 1.2. It is, therefore, apparent that the dominant effect of incorporating Ce into the zirconia lattice is to increase the H_2 adsorption capacity of the oxide. While the physical reason for this effect is not known, we propose that it may be due to increased ability of Ce-O bonds in the oxide to stabilize H atoms as $H^{\delta-}$ and $H^{\delta+}$ species [48, 49].

Catalytic Performance of Cu/m-ZrO_2 and Cu/t´´-$Ce_{0.3}Zr_{0.7}O_2$

The effects of reaction temperature on the activity and selectivity of the 1.2 wt% Cu/m-ZrO_2 and 1.2 wt% Cu/t´´-$Ce_{0.3}Zr_{0.7}O_2$ catalysts are presented in Figure 5. Conversion to methanol increased over the temperature range 473-523 K and was accompanied by a decrease in selectivity. The only major byproduct observed was

methane. These conversion levels are far below the equilibrium values for the given temperatures, which means that the observed rate of methanol formation is not influenced by methanol decomposition. The 1.2wt% Cu/t´´-$Ce_{0.3}Zr_{0.7}O_2$ catalyst exhibited higher conversions to methanol than the m-ZrO_2 supported catalysts over the temperature range studied. For example, the methanol productivity of 1.2 wt% Cu/t´´-$Ce_{0.3}Zr_{0.7}O_2$ was approximately double that of 1.2 wt% Cu/m-ZrO_2 at 523 K. The higher activity of the $Ce_{0.3}Zr_{0.7}O_2$-supported catalyst was also accompanied by a greater selectivity to methanol.

Infrared Spectroscopy Studies

The nature of surface species and the dynamics of CO adsorption and hydrogenation were studied using *in-situ* infrared spectroscopy. Figure 6 shows spectra obtained during CO adsorption on 1.2 wt% Cu/m-ZrO_2 at 523 K. The catalyst was exposed to a flow of 15% CO/He at a total pressure of 0.50 MPa. The bands observed at 1563, 1386, and 1366 cm^{-1} are attributable to the υ_{as}(OCO), δ(CH), and υ_s(OCO) modes, respectively, of b-HCOO-Zr [2, 5, 50-56]. Accompanying features for b-HCOO-Zr in the CH stretching region occur at 2969, 2883 cm^{-1}, and 2748 cm^{-1}, characteristic of (υ_{as}(OCO) + δ(CH)) [49, 50, 53], υ(CH) [2, 5, 46-51], and (υ_s(OCO) + δ(CH)) [54, 57], respectively. C-H stretching features attributed to CH_3O-Zr (2934 and 2830 cm^{-1}) [4, 37, 50, 51, 53, 55, 58, 59] appear almost immediately, even in the absence of gas phase H_2. These features continue to increase for the duration of the CO adsorption experiment (~ 1 h). At the same time, bands at 1039 and 1142 cm^{-1} appear and increase in intensity at a rate similar to that for the bands at 2934 and 2830 cm^{-1}. These peaks are assigned to C-O stretching vibrations of terminal (t-OCH_3) and bridged (b-OCH_3) methoxide species on

ZrO_2, respectively [58, 60, 61]. The shoulder located at approximately 1320 cm^{-1} is assigned to b-CO_3^{2-} -Zr species [41, 56].

Figure 7 shows spectra obtained during CO adsorption on 1.2 wt% $Cu/Ce_{0.3}Zr_{0.7}O_2$ at 523 K. The catalyst was exposed to a flow of 15% CO/He at a total pressure of 0.50 MPa. As with 1.2 wt% Cu/m-ZrO_2, the primary bands are attributable to bidentate formate species with features at 1576, 1379, 1370, 2966, and 2878 cm^{-1}. Each band shifts relative to the position on pure ZrO_2, but bands reported for formate species on CeO_2 are noticeably absent [62-66]. Comparison with Figure 6 shows that formate species are formed at a faster rate on 1.2 wt% $Cu/Ce_{0.3}Zr_{0.7}O_2$. Methoxide species features at 1143, 1040, 2934, and 2828 cm^{-1} are nearly coincident with those observed on 1.2 wt% Cu/m-ZrO_2 and increase over the duration of the transient. In addition to formate and methoxide species, the appearance of broad features between ~ 1550-1450 and 1350-1250 cm^{-1} is indicative of various carbonate and carboxylate species [54, 67], suggesting that the presence of Ce favors the formation of these species. Similar broad bands have been observed after CO adsorption at high temperature on CeO_2 [67].

After CO adsorption for 1 h, transient response spectra were obtained during CO hydrogenation by introducing H_2 into the flowing 15% CO/He (total pressure = 0.50 MPa) so as to achieve a H_2/CO ratio of 3/1. Figure 8 shows spectra obtained on 1.2 wt% Cu/m-ZrO_2 after the switch at 523 K. The features of b-HCOO-Zr at 1564, 1385, and 1367 cm^{-1} decrease rapidly in intensity as soon as H_2 is introduced while, simultaneously, peaks for CH_3O-Zr at 1147 and 1047 cm^{-1} increase rapidly. In the C-H stretching region, bands for CH_3O-Zr increase until they reach a steady-state level after approximately 80 min, analogous to the pattern observed for the corresponding C-O stretching vibrations.

During CO hydrogenation, each C-H stretch red shifts approximately 10-15 cm^{-1} while each of the C-O stretches blue shifts approximately 3-8 cm^{-1}, presumably due to interactions between surface species as surface coverage increases. The δ(CH) feature for CH_3O-Zr (1446 cm^{-1}) [5, 54, 58] is evident initially but remains relatively small throughout the transient.

Figure 9 shows transient response spectra obtained during CO hydrogenation on 1.2 wt% Cu/t´´-$Ce_{0.3}Zr_{0.7}O_2$ at 523 K. Spectra were obtained by introducing H_2 into the flowing 15% CO/He (total pressure = 0.50 MPa) so as to achieve a H_2/CO ratio of 3/1. Upon the introduction of H_2, the broad bands ascribable to carbonate and carboxylate species decrease rapidly. The features for b-HCOO at 1576, 1379, and 1370 cm^{-1} generally decreased over the course of the transient while CH_3O features at 1148, 1061, 2923, and 2816 cm^{-1} increased rapidly and then approached steady-state levels. The υ(CO) mode of terminal CH_3O species is nearly coincident with that observed with m-ZrO_2, but the υ(CO) mode of bridged CH_3O species occurs at a higher wavenumber (1061 cm^{-1} vs. 1047 cm^{-1}). Binet and co-workers [68, 69] have reported C-O stretches of bridged CH_3O species on Ce^{3+} sites at ~ 1080 cm^{-1}. Since H_2-TPR shows that the majority of surface Ce^{4+} cations are reduced to Ce^{3+}, the upward shift of the bridged υ(CO) mode likely reflects the presence of methoxide species bonded to both a Zr^{4+} and Ce^{3+} cation. Consistent with a reduction of most of the Ce atoms in the $Ce_{0.3}Zr_{0.7}O_2$ lattice, no terminal CH_3O was observed on Ce^{4+} cations at ~ 1105 cm^{-1} [68, 69].

A comparison of the evolution of the principle surface species on 1.2 wt% Cu/m-ZrO_2 and 1.2 wt% Cu/t´´-$Ce_{0.3}Zr_{0.7}O_2$ during the CO hydrogenation experiments presented in Figs. 8 and 9 is given in Figure 10. The $\upsilon(CH_3)$ and $\upsilon_{as}(OCO)$ bands were

utilized to track the development of CH_3O-Zr and b-HCOO-Zr species, respectively. Peak areas for both b-HCOO-Zr and CH_3O-Zr were normalized to the value observed after approximately 12 h. The concentration of formate species on 1.2 wt% Cu/m-ZrO_2 decreases rapidly from the level observed in the absence of gas phase H_2 during the first 15 min, before declining more slowly over the remainder of the transient. By contrast, the concentration of formate species goes through a maximum at ~ 3 min on 1.2 wt% Cu/t´´-$Ce_{0.3}Zr_{0.7}O_2$ before decreasing more slowly over the course of the experiment. The maximum in formate concentration is attributed to the rapid hydrogenation of surface carbonate and/or carboxylate species to produce new formate groups, evidenced by the rapid decline in the broad bands at ~ 1550-1450 and 1350-1250 cm^{-1}. Hydrogenation of carbonate species to formate species has previously been observed during studies of CO_2 hydrogenation on Cu/ZrO_2 [70]. On both catalysts, the concentration of methoxide species increases rapidly from the levels observed during CO adsorption, reaching values within 95% of the steady-state concentration in < 1 h.

The relative rates of consumption of formate and methoxide species was examined by switching from a CO/H_2 mixture to one containing only H_2. Figure 11 compares the dynamics of consumption of b-HCOO-Zr and CH_3O-Zr species on 1.2 wt% Cu/m-ZrO_2 and 1.2 wt% Cu/t´´-$Ce_{0.3}Zr_{0.7}O_2$. Transient response spectra were obtained by replacing the 15% CO/He in the 3/1 H_2/CO flow with He while maintaining the total pressure at 0.50 MPa. Peak areas for both b-HCOO-Zr and CH_3O-Zr are normalized to the value observed at the beginning of the transient. b-HCOO species decreased more rapidly initially on 1.2 wt% Cu/m-ZrO_2, though the overall decrease in intensity is similar for both materials at the end of the transient. The concentration of CH_3O species

decreases more rapidly on 1.2 wt% Cu/t´´-$Ce_{0.3}Zr_{0.7}O_2$ than on 1.2 wt% Cu/m-ZrO_2, and there is significant disparity in the relative concentration of these species at the conclusion of the 6 h experiment. The initial decrease in methoxide species intensity also occurs after a shorter time on 1.2 wt% Cu/t´´-$Ce_{0.3}Zr_{0.7}O_2$ (~ 2.5 min) than on 1.2 wt% Cu/m-ZrO_2 (~ 4 min) (see Fig. 11(c)). The apparent first-order rate constant for the removal of methoxide species, k_{app}, determined from the initial portion of the transient is 4.1×10^{-3} min^{-1} and 1.0×10^{-2} min^{-1} for 1.2 wt% Cu/m-ZrO_2 and 1.2 wt% Cu/t´´-$Ce_{0.3}Zr_{0.7}O_2$, respectively.

Figure 12 shows the evolution of the O-H stretching region for both 1.2 wt% Cu/m-ZrO_2 and 1.2 wt% Cu/t´´-$Ce_{0.3}Zr_{0.7}O_2$ during the H_2 reduction experiments presented in Figure 10. Each material exhibits hydroxyl group consumption bands at ~ 3728 cm^{-1} and ~ 3670 cm^{-1} at the conclusion of CO hydrogenation (t = 0 in Fig. 12). After the switch to an H_2-only feed, the bands decrease in negative absorbance with progressing time, indicating a net recovery of hydroxyl groups over the course of the experiment. This is consistent with removal of formate and methoxide groups adsorbed at these sites during reaction through hydrogenation to methanol [5]. Notably, a greater portion of the hydroxyl groups on 1.2 wt% Cu/t´´-$Ce_{0.3}Zr_{0.7}O_2$ was recovered during the course of the transient. Based on the changes in peak intensity, ~ 35% and ~ 75% of hydroxyl groups are recovered after 6 h on 1.2 wt% Cu/m-ZrO_2 and 1.2 wt% Cu/t´´-$Ce_{0.3}Zr_{0.7}O_2$, respectively. These values agree well with the fraction of methoxide species removed during the same experiment (see Fig. 12) (~ 42% on 1.2 wt% Cu/m-ZrO_2 and ~ 78% on 1.2 wt% Cu/t´´-$Ce_{0.3}Zr_{0.7}O_2$), and suggest that most of the recovery in OH band intensity is associated with the removal of methoxide groups. Such a result would be

expected from a consideration of the relative intensities of the band intensities for methoxide and formate species (see Figs. 8 and 9).

In their studies of methanol synthesis over Cu/t-ZrO_2 and Cu/m-ZrO_2 Bell and co-workers [13] established that the rate limiting step is reductive elimination of Zr-OCH_3 species. As a result, the observed rate of methanol synthesis is proportional to the product of the apparent first order rate coefficient for methoxide reductive elimination, k_{app}, and the surface concentration of methoxide groups, θ_{CH_3O}. The same reasoning can be used to interpret the higher rate of methanol synthesis on Cu/t´´- $Ce_{0.3}Zr_{0.7}O_2$ relative to Cu/m-ZrO_2 observed in the present study. The values of k_{app} based on the initial data of the transient shown in Figures 11(b) and (c) are 4.1×10^{-3} min^{-1} and 1.0×10^{-2} min^{-1} for 1.2 wt% Cu/m-ZrO_2 and 1.2 wt% Cu/t´´-$Ce_{0.3}Zr_{0.7}O_2$, respectively. Hence, the apparent rate coefficient is 2.4 higher for 1.2 wt% Cu/t´´-$Ce_{0.3}Zr_{0.7}O_2$ than 1.2 wt% Cu/m-ZrO_2. The higher value of k_{app} for the former catalyst is quite possibly due to the higher H_2 adsorption capacity of t´´-$Ce_{0.3}Zr_{0.7}O_2$, since k_{app} is the product of the intrinsic rate coefficient for reductive elimination and the coverage of the oxide surface by H atoms. If it assumed that the intrinsic rate coefficients on both catalysts are the same then the observed ratio of apparent coefficients would imply a 2.9 (corrected for the ratios of oxide surface areas) higher H-atom coverage on t´´-$Ce_{0.3}Zr_{0.7}O_2$, which is consistent with the measured ratio in H_2 adsorption capacities, 3.3. Based on the peak areas of the terminal and bridged methoxide C-O stretches, the ratio of methoxide species adsorbed on $Ce_{0.3}Zr_{0.7}O_2$ relative to ZrO_2 is 1.3 (corrected for the ratios of oxide surface areas) under steady-state reaction conditions. Hence, the ratio of the product $k_{app}\cdot\theta_{CH_3O}$ is ~ 3.8 in favor of 1.2 wt% Cu/t´´-$Ce_{0.3}Zr_{0.7}O_2$. This figure is in reasonable agreement with the

observed ratio of methanol synthesis activities, ~ 2.7, once the measured rates are corrected for differences in the surface areas of the oxide and the dispersed Cu.

Conclusions

The activity for methanol synthesis from CO and H_2 of Cu/t´´-$Ce_{0.3}Zr_{0.7}O_2$ is approximately two-fold higher than that for Cu/m-ZrO_2, assuming the same surface areas of the oxides and the dispersed Cu. While Ce^{4+} cations replace Zr^{4+} cations isomorphously in the zirconia lattice during synthesis, the substituted cations are readily reducible to Ce^{3+}. The presence of Ce increases the adsorption capacity of the oxide for H atoms produced by dissociative adsorption of H_2 on the dispersed particles of Cu and spillover onto the oxide surface. The concentration of adsorbed methoxide species is also somewhat higher when Ce is substituted into the zirconium lattice. These two factors appear to account for the higher activity of Cu/t´´-$Ce_{0.3}Zr_{0.7}O_2$.

Acknowledgment

This work was supported by the Director, Office of Basic Energy Sciences, Chemical Sciences Division of the U.S. Department of Energy under Contract DE-AC03-76SF00098.

References

1. Saussey, J., and Lavalley, J.C., *J. Mol. Catal.* **50**, 343 (1989).

2. Schild, C., Wokaun, A., and Baiker, A., *J. Mol. Catal.* **63**, 243 (1990).

3. Fujita, S., Usui, M., Ito, H., and Takezawa, N., *J. Catal.* **157**, 403 (1995).

4. Weigel, J., Koeppel, R.A., Baiker, A., and Wokaun, A., *Langmuir* **12**, 5319 (1996).

5. Fisher, I.A., and Bell, A.T., *J. Catal.* **178**, 153 (1998).

6. Meitzner, G., and Iglesia, E., *Catal. Today* **53**, 433 (1999).

7. Denise, B., and Sneeden, R.P.A., *Appl. Catal.* **28**, 235 (1986).

8. Sun, Y., and Sermon, P.A., *J. Chem. Soc. Commun.* 1242 (1993).

9. Sun, Y., and Sermon, P.A., *Catal. Lett.* **29**, 361 (1994).

10. Fisher, I.A., Woo, H.C., and Bell, A.T., *Catal. Lett.* **44**, 11 (1997).

11. Suh, Y.W., Moon, S.H., and Rhee, H.K., *Catal. Today* **63**, 447 (2000).

12. Rhodes, M.D., and Bell, A.T., *J. Catal.* **233**, 198 (2005).

13. Rhodes, M.D., Pokrovski, K.A., and Bell, A.T., *J. Catal.* 233, 210 (2005).

14. Ozawa, M., *J. Alloys Comp.* **275-277**, 886 (1998).

15. Kašpar, J., Fornasiero, P., and Graziani, M., *Catal. Today* **50**, 285 (1999).

16. Masui, T., Ozaki, T., Machida, K., and Adachi, G., *J. Alloys Comp.* **303-304**, 49 (2000).

17. Mamontov, E., Egani, T., Brezny, R., Korrane, M., and Tyagi, S., *J. Phys. Chem. B* **104**, 11110 (2000).

18. Kašpar, J., and Fornasiero, P., *J. of Solid State Chem.* **171**, 19 (2003).

19. Daturi, M., Finocchio, E., Binet, C., Lavalley, J.C., Fally, F., Perrichon, U., Vidal, H., Hickey, N., and Kašpar, J., *J. Phys. Chem. B* **104**, 9186 (2000).

20. Vilac., G., Di Monte, R., Fornasiero, P., Fonda, E., Kašpar, J., and Graziani, M., *in* "Studies in Surface Science and Catalysis: Catalysis and Automotive Pollution Control IV", Vol. 116. Elsevier, Amsterdam, 1998.

21. Toby, B.H., *J. Appl. Cryst.* **34**, 210-213 (2001).

22. Sato, S., Takahashi, R., Sodesawa, T., Yuma, K., and Obata, Y., *J. Catal.* **196**, 195 (2000).

23. Sorenson, K.J., and Cant, N.W., *Catal. Lett.* **33**, 117 (1995).

24. Hicks, R.F., Kellner, C.S., Savatsky, B.J., Hecker, W.C., and Bell, A.T., *J. Catal.* **71**, 216 (1981).

25. Hori, C.E., Permana, H., Simon Ng, K.Y., Brenner, A., More, K., Rahmoeller, K.M., and Belton, D.N., *Appl. Catal. B: Environ.* **16**, 105 (1998).

26. Bozo, C., Gaillard, F., and Guilhaume, N., *Appl. Catal. A: Gen.* **220**, 69 (2001).

27. Tani, E., Yoshimura, M., and Smiya, S., *J. Am. Ceram. Soc.* **66**, 506 (1983).

28. Duran, P., Gonzales, M., Moure, C., Jurdo, J.R., and Pascal, C., *J. Mater. Sci.* **25**, 5001 (1990).

29. Yashima, M., Arashi, H., Kakihana, M., and Yoshimura, M., *J. Am. Ceram. Soc.* **77**, 1067 (1994).

30. Yashima, M., Morimoto, K., Ishizawa, N., and Yoshimura, M., *J. Am. Ceram. Soc.* **76**, 1745 (1993).

31. Yashima, M., Morimoto, K., Ishizawa, N., and Yoshimura, M., *J. Am. Ceram. Soc.* **77**, 2865 (1993).

32. Ferraro, J.R., and Nakamoto, K., *in* "Introductory Raman Spectroscopy". Academic Press, New York, 1994.

33. Schild, C., Wokaun, A., Koeppel, R.A., and Baiker, A., *J. Catal.* **130**, 657 (1991).

34. Li, M., Feng, Z., Xiong, G., Ying, P., Xin, Q., and Li, C., *J. Phys. Chem. B* **105**, 8107 (2001).

35. Li, C., and Li, M., *J. Raman Spectrosc.* **33**, 301 (2002).

36. Trovarelli, A., Zamar, F., Lorca, J., Leitenburg, C., Dolcetti, G., and Kiss, J.T., *J. Catal.* **169**, 490 (1997).

37. Escribano, V.S., López, E.F., Panizza, M., Resini, C., Amores, J.M.G., and Busca, G., *Solid State Sciences* **5**, 1369 (2003).

38. Fornasiero, P., Balducci, G., Di Monte, R., Kašpar, J., Sergo, V., Gubitosa, G., Ferrero, A., and Graziani, M., *J. Catal.* **164**, 173 (1996).

39. Enzo, S., Delogu, F., Frattini, R., Primavera, A., and Trovarelli, A., *J. Mater. Res.* **15**, 1538 (2000).

40. Martin, D., and Duprez, D., *J. Phys. Chem. B* **101**, 4428 (1997).

41. Jung, K.D., and Bell, A.T., *J. Catal.* **193**, 207 (2000).

42. Shimokawabe, M., Asakawa, H., and Takezawa, N., *Appl. Catal.* **59**, 45 (1990).

43. Zhou, R., Yu, T., Jiang, X., Chen, F., and Zheng, X., *Appl. Surf. Sci.* **148**, 263 (1999).

44. Trovarelli, A., Dolcetti, G., de Leitenburg, C., Kašpar, J., Finetti, P., and Santoni, A., *J. Chem. Soc., Faraday Trans.* **88**, 1311 (1992).

45. Bernal, S., Calvino, J.J., Cifredo, G.A., Laachir, A., Perrichon, V., and Herrmann, J.M., *Langmuir* **10**, 717 (1994).

46. de Leitenburg, C., Trovarelli, A., and Kašpar, J., *J. Catal.* **166**, 98 (1997).

47. Boaro, M., Vicaro, M., de Leitenburg, C., Dolcetti, G., and Trovarelli, A., *Catal. Today* **77**, 407 (2003).

48. Lamonier, C., Ponchel, A., D'Huysser, A., and Jalowiecki-Duhamel, L., *Catal. Today* **50**, 247 (1999).

49. Fierro, J.L.G., Soria, J., Sanz, J., and Rojo, J.M., *J. of Solid State Chem.* **66**, 154 (1987).

50. He, M.Y., and Ekerdt, J.G., *J. Catal.* **87**, 381 (1984).

51. Kondo, J., Abe, H., Sakata, Y., Maruya, K., Domen, K., and Onishi, T., *J. Chem. Soc., Faraday Trans. 1* **84**, 511 (1988).

52. Hertl, W., *Langmuir* **5**, 96 (1989).

53. Guglielminotti, E., *Langmuir* **6**, 1455 (1990).

54. Bianchi, D., Chafik, T., Khalfallah, M., and Teichner, S.J., *Appl. Catal. A: Gen.* **105**, 223 (1993).

55. Kalies, H., Pinto, N., Pajonk, G.M., and Bianchi, D., *Appl. Catal. A: Gen.* **202**, 197 (2000).

56. Pokrovski, K., Jung, K.T., and Bell, A.T., *Langmuir* **17**, 4297 (2001).

57. Edwards, J., and Schrader, G., *J. Phys. Chem.* **89**, 782 (1985).

58. Bensitel, M., Moravek, V., Lamonte, J., Saur, O., and Lavalley, J.C., *Spectrochimica Acta.* **43a**, 1487 (1987).

59. Bianchi, D., Chafik, T., Khalfallah, M., and Teichner, S.J., *Appl. Catal. A: Gen.* **123**, 89 (1995).

60. Ouyang, F., Kondo, J.N., Maruya, K., and Domen, K., *J. Phys. Chem. B* **101**, 4867 (1997).

61. Ouyang, F., Kondo, J.N., Maruya, K., and Domen, K., *Catal. Lett.* **50**, 179 (1998).

62. Li, C., Sakata, Y., Arai, T., Domen, K., Maruya, K., and Onishi, T., *J. Chem. Soc., Faraday Trans. 1* **85**, 929 (1989).

63. Shido, T., and Iwasawa, Y., *J. Catal.* **141**, 71 (1993).

64. Finocchio, E., Daturi, M., Binet, C., Lavalley, J.C., and Blanchard, G., *Catal. Today* **52**, 53 (1999).

65. Jacobs, G., Williams, L., Graham, U., Thomas, G.A., Sparks, D.E., and Davis, B.H., *Appl. Catal. A: Gen.* **252**, 107 (2003).

66. Jacobs, G., Patterson, P.M., Williams, L., Chenu, E., Sparks, D., Thomas, G., and Davis, B.H., *Appl. Catal. A: Gen.* **262**, 177 (2004).

67. Li, C., Sakata, Y., Arai, T., Domen, K., Maruya, K., and Onishi, T., *J. Chem. Soc., Faraday Trans. 1* **85**, 1451 (1989).

68. Badri, A., Binet, C., and Lavalley, J.C., *J. Chem. Soc., Faraday Trans.* **93**, 1159 (1997).

69. Binet, C., and Daturi, M., *Catal. Today* **70**, 155 (2001).

70. Fisher, I.A., and Bell, A.T., *J. Catal.* **172**, 222 (1997).

71. Table 1. Cu surface area and exchangeable H for 1.2 wt% Cu/m-ZrO_2 and 1.2 wt% Cu/$Ce_{0.3}Zr_{0.7}O_2$.

Sample	Cu Surface Area (m^2/g)	Cu Dispersion (%)	Exchangable H ($\mu mol/m^2$)
1.2 wt% Cu/m-ZrO_2	0.87	11.1	10.9
1.2 wt% Cu/$Ce_{0.3}Zr_{0.7}O_2$	0.73	9.3	7.8

Table 2. Effect of Ce incorporation on the adsorption capacity and binding strength of CO at 523 K.

Sample	CO desorbed ($\mu mol/m^2$)	Peak Max. T (K)	CO_2 desorbed ($\mu mol/m^2$)	Peak Max. T (K)	Total CO_x desorbed ($\mu mol/m^2$)	H_2 desorbed ($\mu mol/m^2$)
1.2 wt% Cu/m-ZrO_2	0.51	620	0.77	590, 675	1.28	0.26
1.2 wt% Cu/$Ce_{0.3}Zr_{0.7}O_2$	0.94	575, 615	0.60	635	1.54	0.87

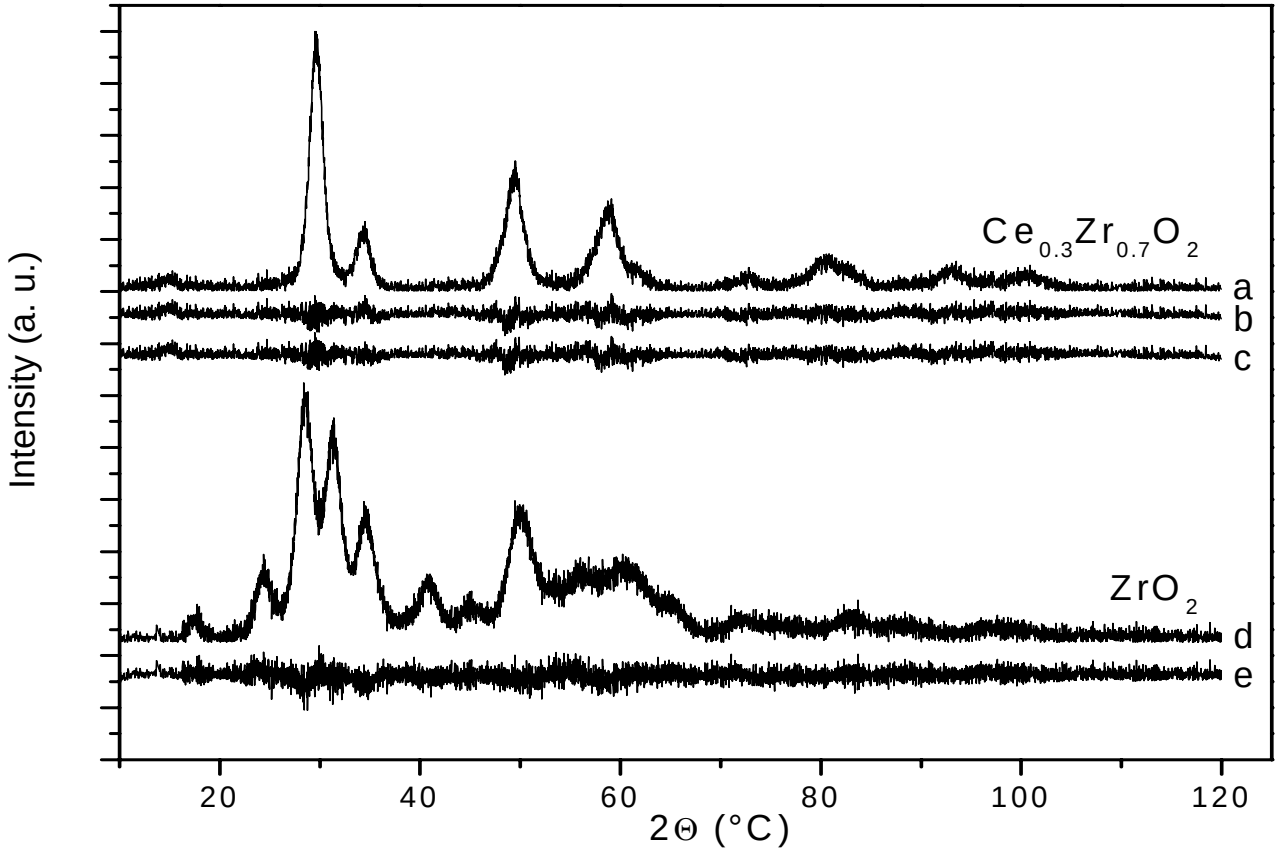

Figure 1. XRD patterns for ZrO_2 and $Ce_{0.3}Zr_{0.7}O_2$.

(a –observed profile for $Ce_{0.3}Zr_{0.7}O_2$, b and c – difference between observed and calculated profiles in cubic symmetry, *Fm*3*m* space group, and tetragonal symmetry, $P4_2/nmc$ space group, respectively; d- observed profile for ZrO_2 and e – difference between observed and calculated profiles in monoclinic symmetry $P2_1/c$ space group)

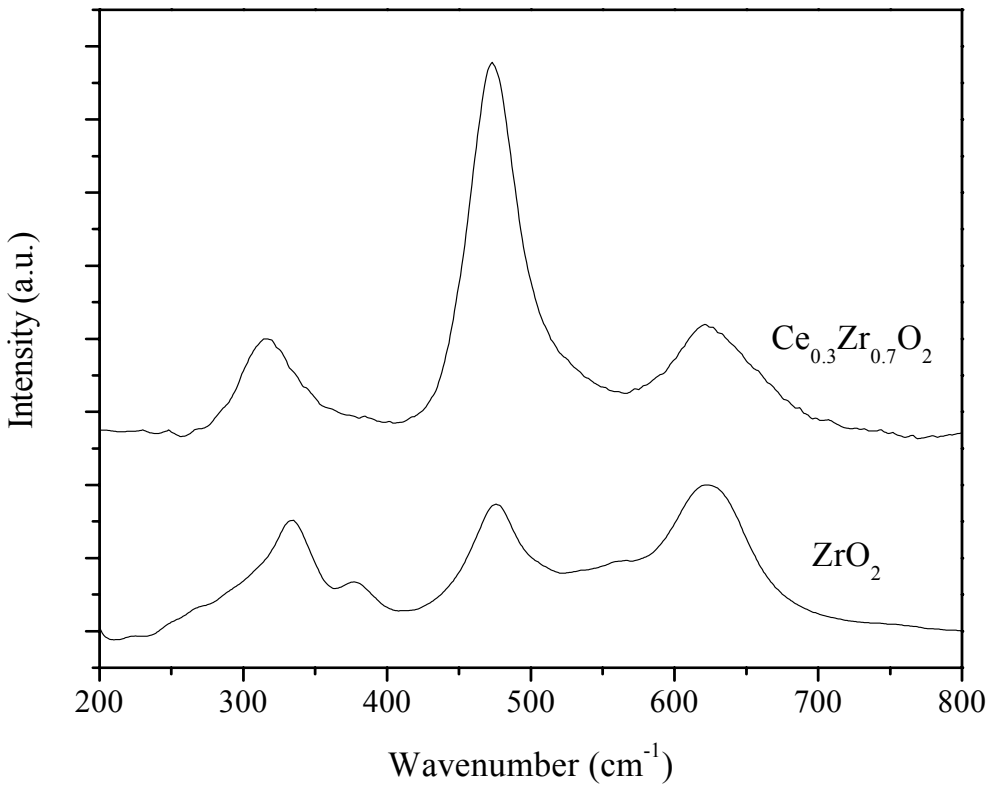

Figure 2. Raman spectra for ZrO_2 and $Ce_{0.3}Zr_{0.7}O_2$ at room temperature.

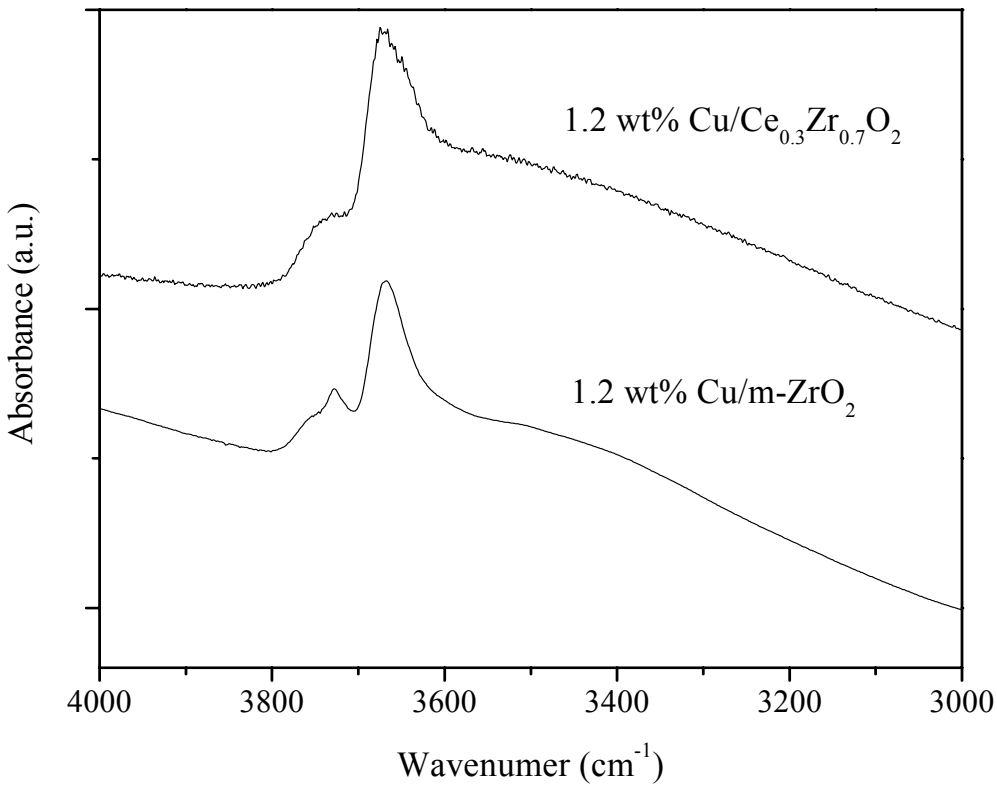

Figure 3. Infrared spectra of the hydroxyl group stretching region taken for 1.2 wt% Cu/ZrO_2 and 1.2 wt% $Cu/Ce_{0.3}Zr_{0.7}O_2$ following calcination and reduction. Spectra referenced to empty cell in He.

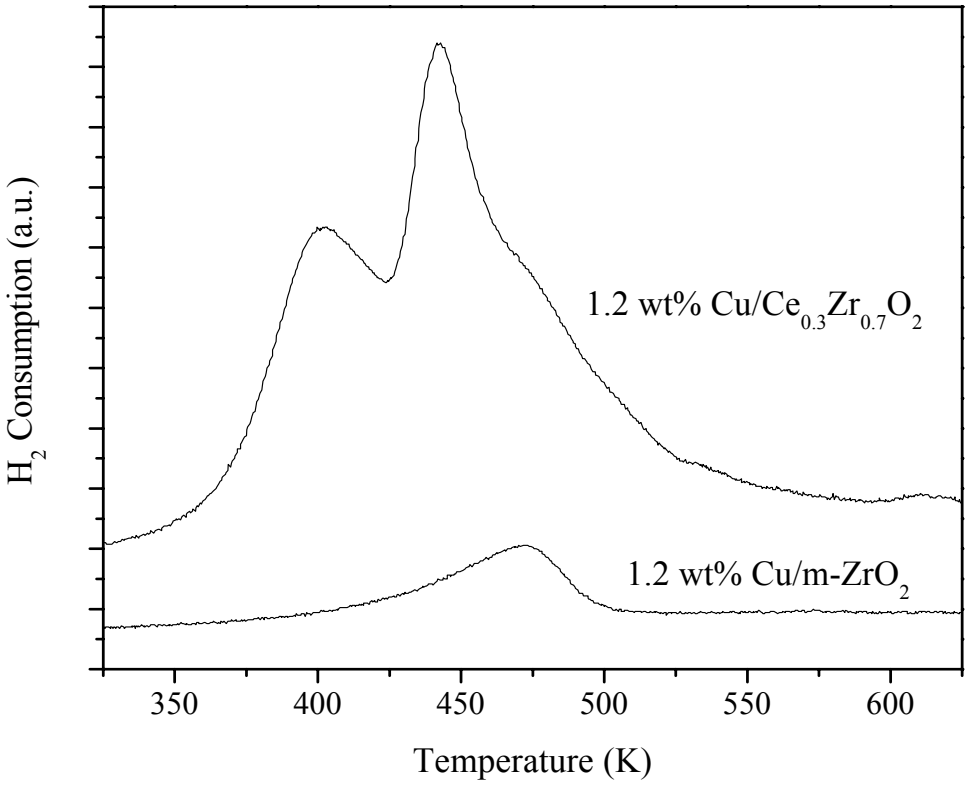

Figure 4. H_2-TPR spectra for 1.2 wt% Cu/m-ZrO2 and 1.2 wt% $Cu/Ce_{0.3}Zr_{0.7}O_2$. Heating rate = 20 K/min; 2% H_2/He flow rate = 60 cm^3/min.

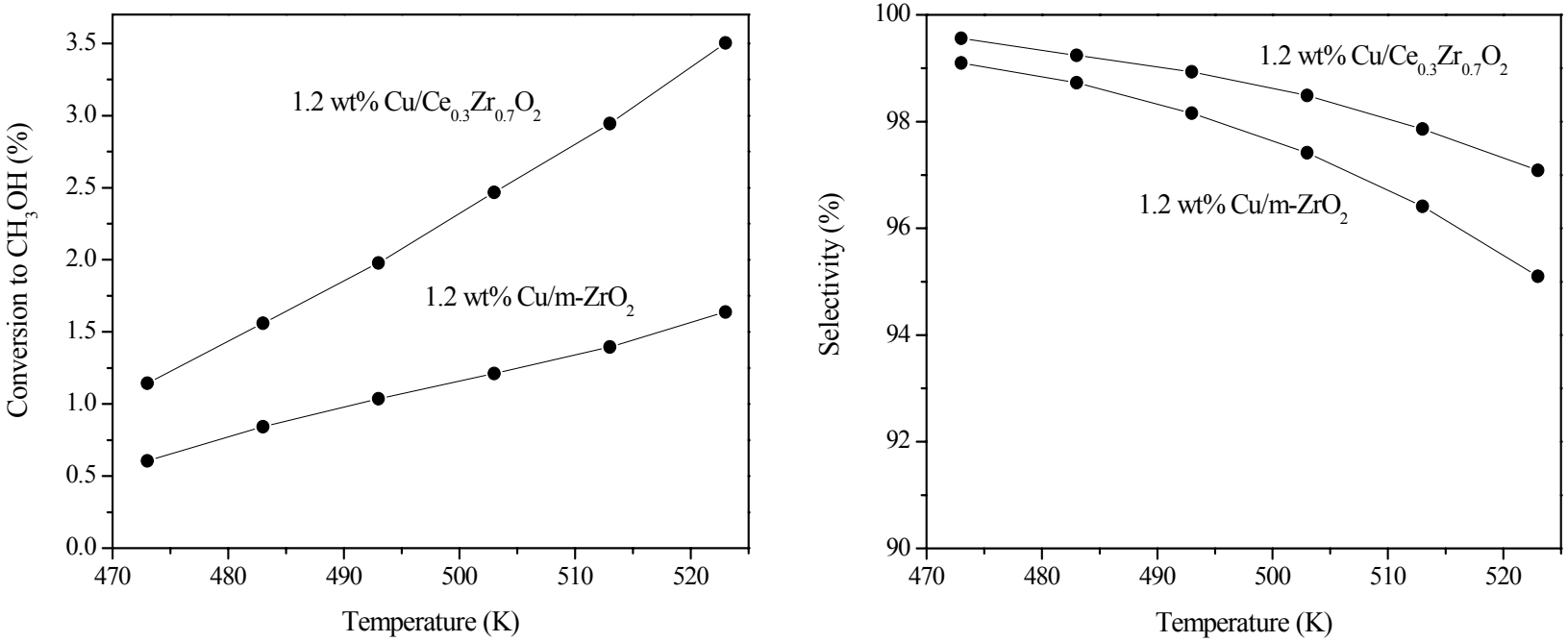

Figure 5. Effect of temperature on the selective conversion (a) and overall selectivity (b) of CO to methanol during CO hydrogenation: catalyst mass = 0.15 g; P = 3.0 MPa; $H_2/CO = 3$; total flow rate = 60 cm^3/min.

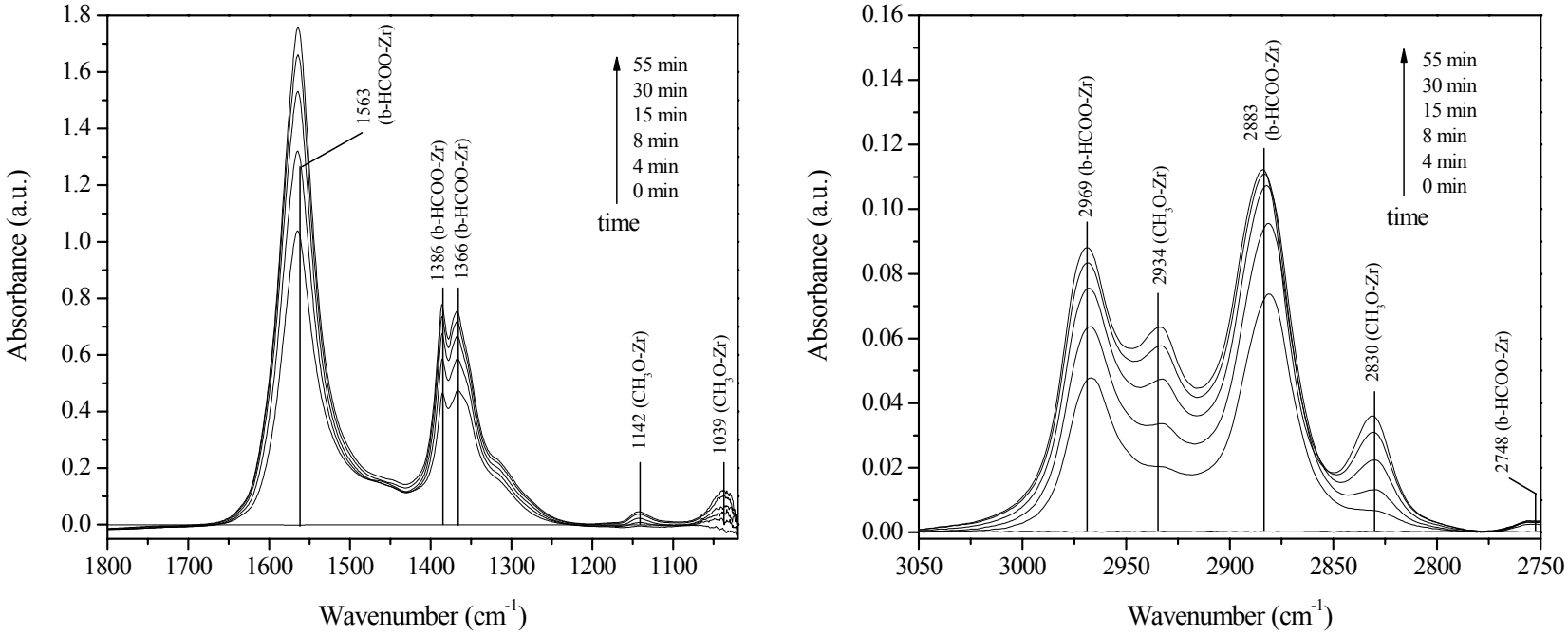

Figure 6. Infrared spectra taken for 1.2 wt% Cu/m-ZrO_2 at 523 K after switching feed from 0.50 MPa He to 0.05 MPa CO and 0.45 MPa He flowing at a total rate of 60 cm^3/min. Spectra referenced to 1.2 wt% Cu/m-ZrO_2 under 0.50 MPa He flow at 523 K.

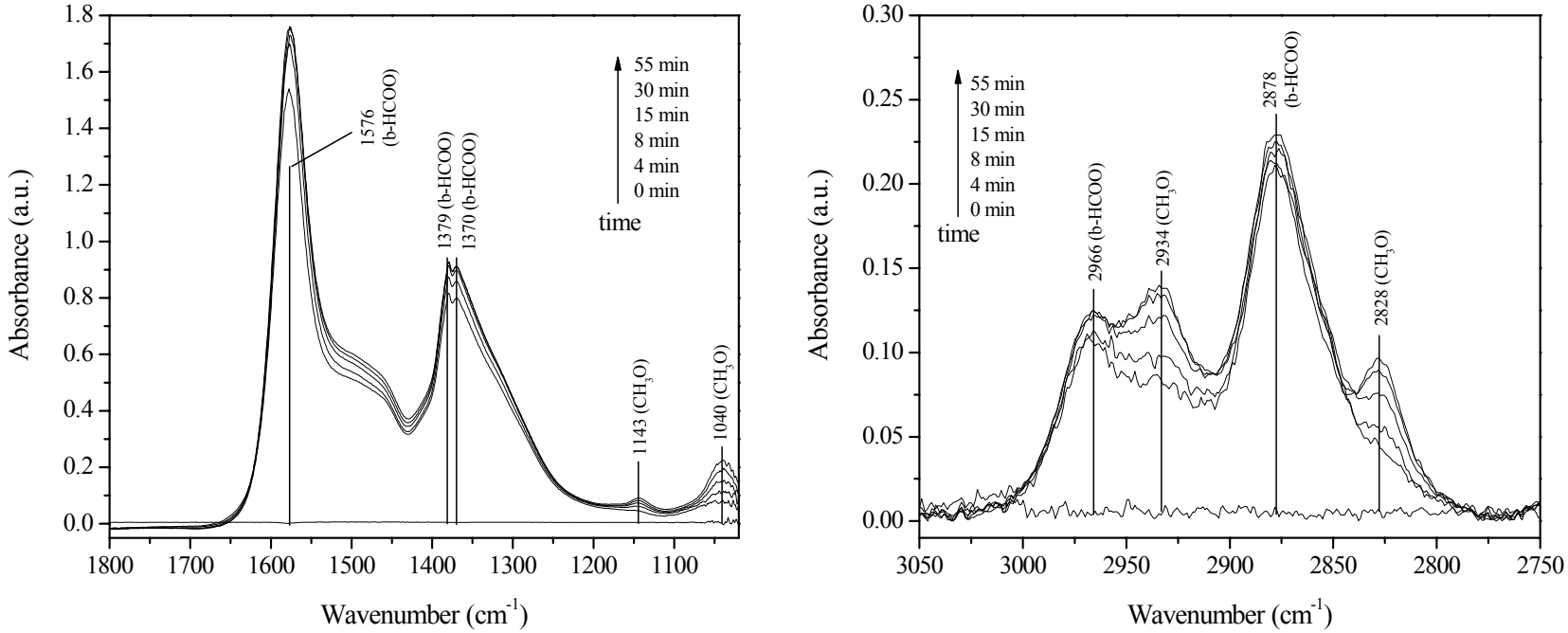

Figure 7. Infrared spectra taken for 1.2 wt% $Cu/Ce_{0.3}Zr_{0.7}O_2$ at 523 K after switching feed from 0.50 MPa He to 0.05 MPa CO and 0.45 MPa He flowing at a total rate of 60 cm^3/min. Spectra referenced to 1.2 wt% $Cu/Ce_{0.3}Zr_{0.7}O_2$ under 0.50 MPa He flow at 523 K.

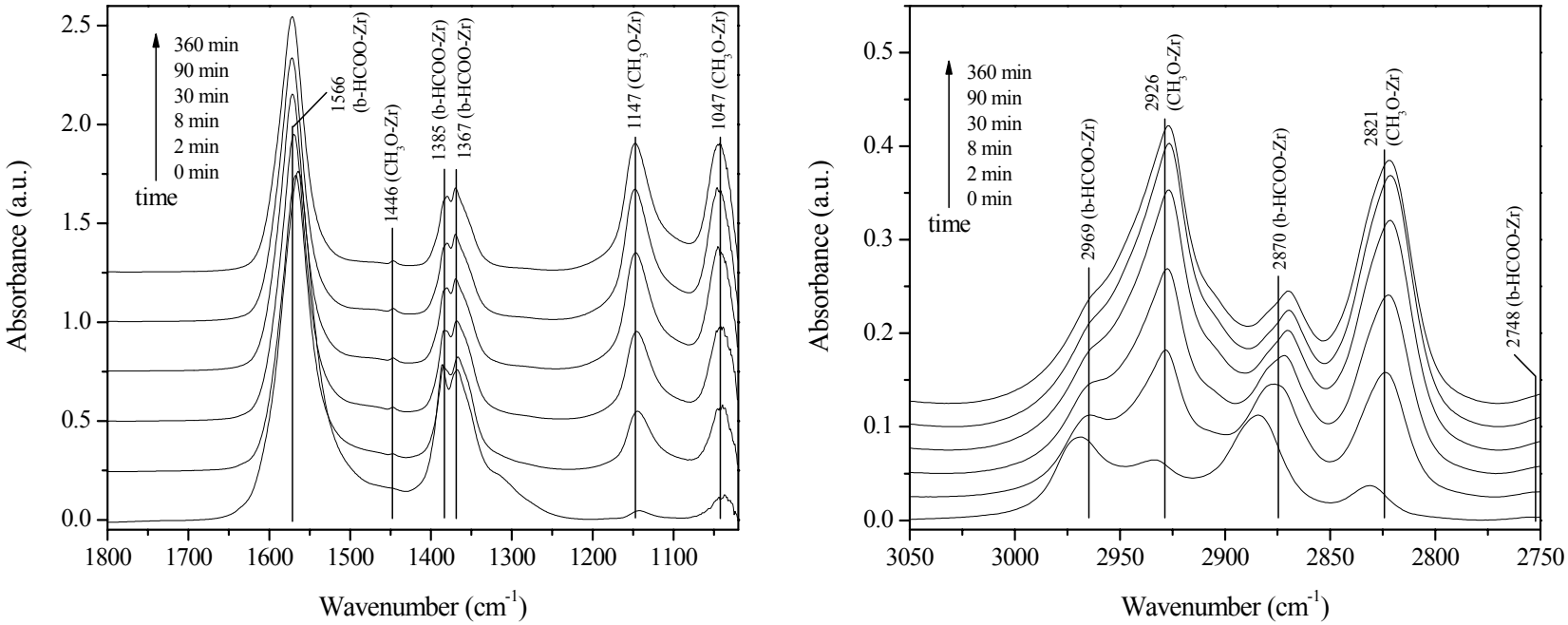

Figure 8. Infrared spectra taken for 1.2 wt% Cu/m-ZrO_2 at 523 K after switching feed from 0.05 MPa CO and 0.45 MPa He to 0.05 MPa CO, 0.15 MPa H_2, and 0.30 MPa He flowing at a total rate of 60 cm^3/min. Spectra referenced to 1.2 wt% Cu/m-ZrO_2 under 0.50 MPa He flow at 523 K.

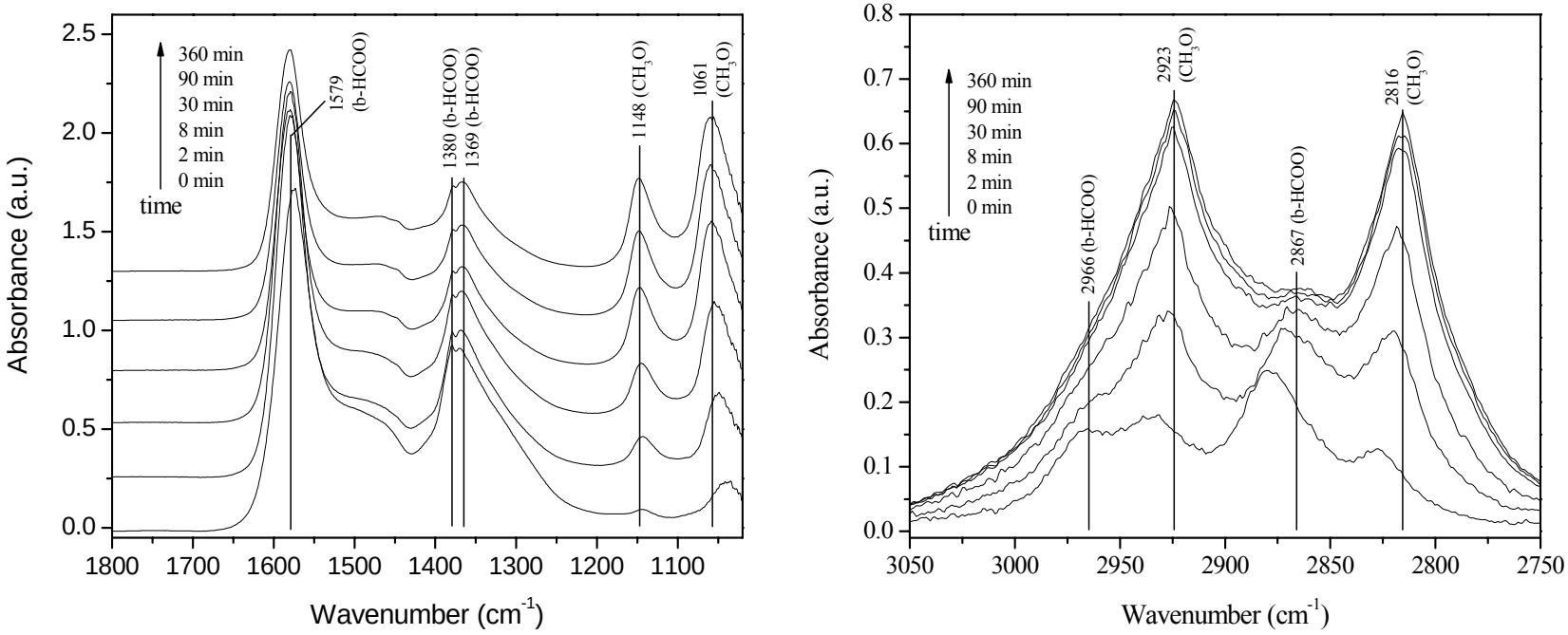

Figure 9. Infrared spectra taken for 1.2 wt% $Cu/Ce_{0.3}Zr_{0.7}O_2$ at 523 K after switching feed from 0.05 MPa CO and 0.45 MPa He to 0.05 MPa CO, 0.15 MPa H_2, and 0.30 MPa He flowing at a total rate of 60 cm^3/min. Spectra referenced to 1.2 wt% $Cu/Ce_{0.3}Zr_{0.7}O_2$ under 0.50 MPa He flow at 523 K.

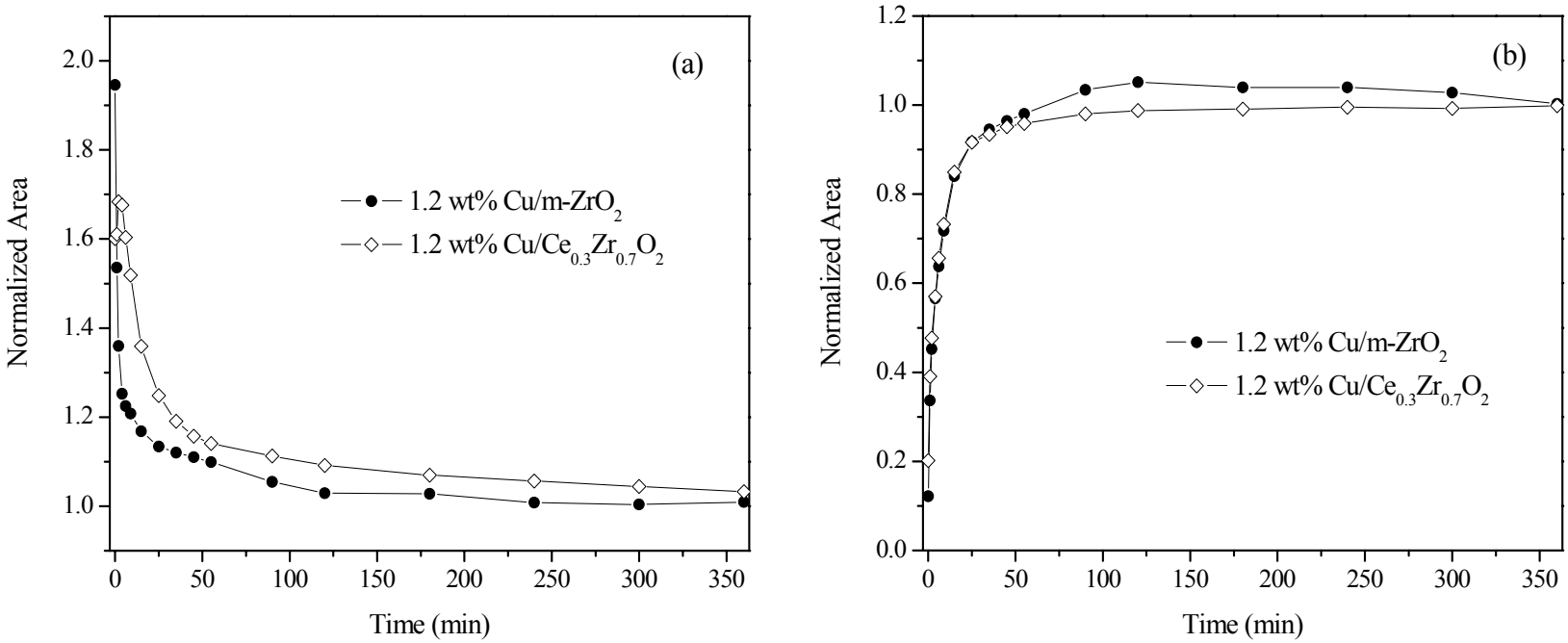

Figure 10. Peak Areas of (a) b-HCOO-Zr and (b) CH_3O-Zr features for 1.2 wt% Cu/m-ZrO_2 and 1.2 wt% Cu/$Ce_{0.3}Zr_{0.7}O_2$ during the experiments in Figs. 5.9 and 5.10. Areas normalized to the values observed at the end of the transient.

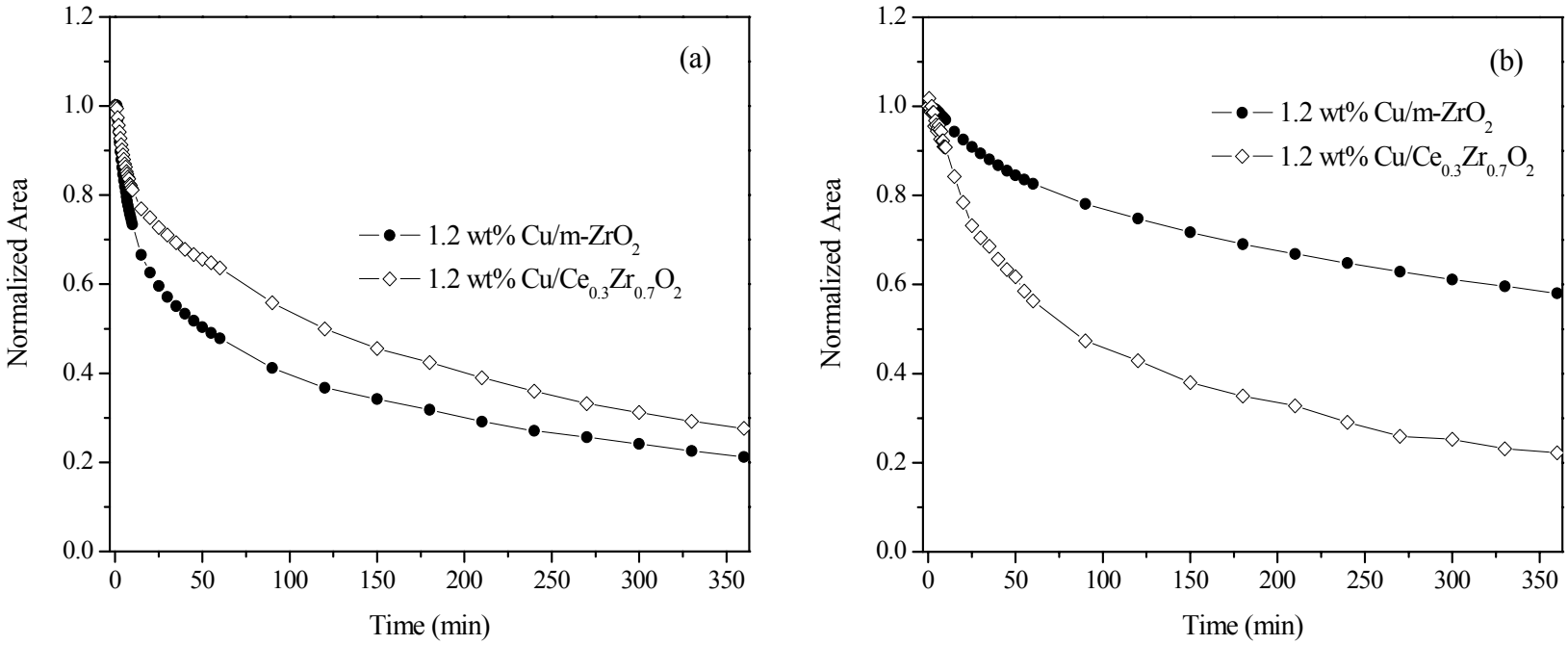

Figure 11. Peak Areas of (a) b-HCOO-Zr and (b) CH_3O-Zr features for 1.2 wt% Cu/m-ZrO_2 and 1.2 wt% Cu/$Ce_{0.3}Zr_{0.7}O_2$ at 523 K after switching feed from 0.05 MPa CO, 0.15 MPa H_2, and 0.30 MPa He to 0.15 MPa H_2 and 0.35 MPa He flowing at a total rate of 60 cm^3/min. Areas normalized to the values observed at the beginning of the transient.

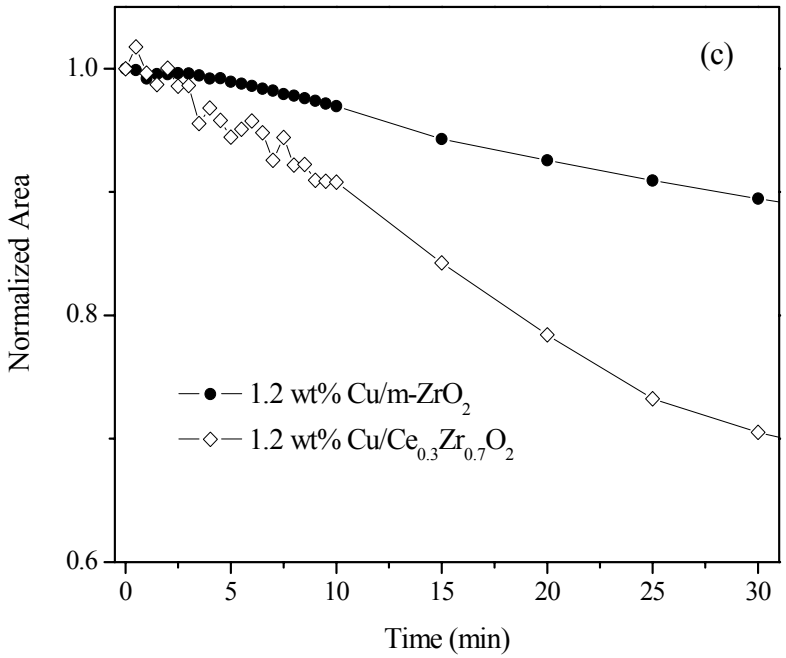

Figure 11. Peak Areas of (c) CH_3O-Zr features for 1.2 wt% Cu/m-ZrO_2 and 1.2 wt% $Cu/Ce_{0.3}Zr_{0.7}O_2$ at 523 K after switching feed from 0.05 MPa CO, 0.15 MPa H_2, and 0.30 MPa He to 0.15 MPa H_2 and 0.35 MPa He flowing at a total rate of 60 cm^3/min. Areas normalized to the values observed at the beginning of the transient.

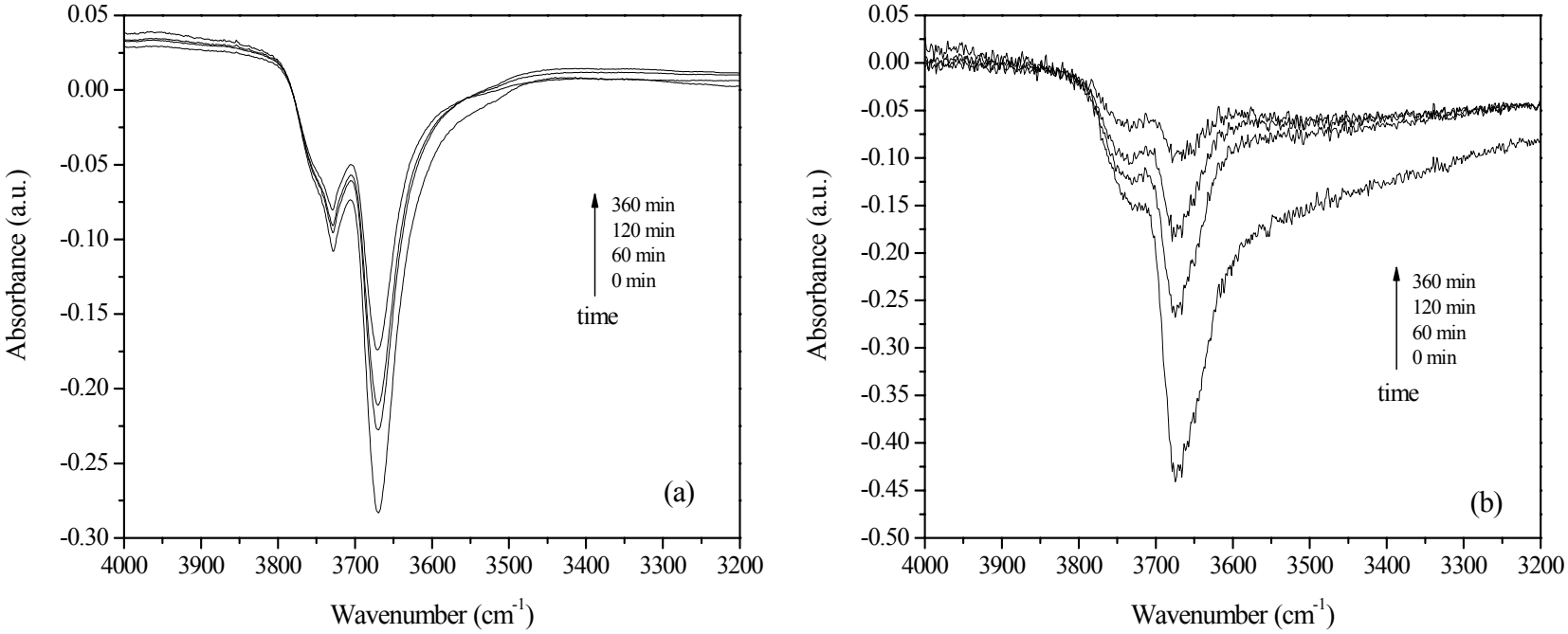

Figure 12. Infrared spectra taken for (a) 1.2 wt% Cu/m-ZrO_2 and (b) 1.2 wt% $Cu/Ce_{0.3}Zr_{0.7}O_2$ at 523 K after switching feed from 0.05 Mpa CO, 0.15 MPa H_2, and 0.45 MPa He to 0.15 MPa H_2 and 0.35 MPa He flowing at a total rate of 60 cm^3/min. Spectra referenced to 1.2 wt% Cu/m-ZrO_2 and 1.2 wt% $Cu/Ce_{0.3}Zr_{0.7}O_2$ under 0.50 MPa He flow at 523 K, respectively.